21st AIAA Fluid Dynamics Conference
June 24-27, 2013, San Diego, CA

Functional Equivalence Acceptance Testing of FUN3D for Entry Descent and Landing Applications

Peter A Gnoffo*
William A Wood†, Bil Kleb‡
Stephen Alter§, Chris Glass¶, Jose Padilla‖
Dana Hammond**, Jeffery White††
NASA Langley Research Center, Hampton, VA 23681-2199

The functional equivalence of the unstructured grid code FUN3D to the the structured grid code LAURA (Langley Aerothermodynamic Upwind Relaxation Algorithm) is documented for applications of interest to the Entry, Descent, and Landing (EDL) community. Examples from an existing suite of regression tests are used to demonstrate the functional equivalence, encompassing various thermochemical models and vehicle configurations. Algorithm modifications required for the node-based unstructured grid code (FUN3D) to reproduce functionality of the cell-centered structured code (LAURA) are also documented. Challenges associated with computation on tetrahedral grids versus computation on structured-grid derived hexahedral systems are discussed.

I. Introduction

The simulation of aerothermodynamic environments of entry vehicles within NASA over the past two decades have been executed with two independently developed codes. The Langley Aerothermodynamic Upwind Relaxation Algorithm (LAURA)[1] was first utilized in 1987 for simulations of a proposed Aeroassist Flight Experiment (AFE) vehicle[2] and later was extensively used in defining the aerothermodynamic database for the Mars Pathfinder. The Data Parallel Line Relaxation Code (DPLR),[3] initially developed at the University of Minnesota and later adopted and expanded at NASA Ames, has been utilized in parallel for defining vehicle entry environments. Both codes have been used for every NASA mission involving atmospheric entry since Mars Pathfinder, including the Space Shuttle and in the analysis of vehicle programs including X-33, X-34, X-37 through to the present Multi-Purpose Crew Vehicle (MPCV). Teams at Langley and Ames have benefited over the years by the ability to cross check and correct independently developed algorithms and physical models used in the two codes – a highly valued capability in situations where extrapolation from limited ground-based experimental validation to flight conditions is extremely challenging.

Both LAURA and DPLR are multi-block structured grid codes. Their ability to define aerothermal environments around protuberances, scarfed nozzles with jets firing, and other small scale irregularities on an otherwise "smooth" vehicle surface generally requires significant investment of time to generate appropriate grids. (Overset grid approaches in DPLR alleviate these challenges but still require careful grid generation to accommodate resolution of flow topologies ensuing from local interactions.) Unstructured grid algorithms offer greater flexibility in both defining complex geometric features and in adapting the grid to the shocks,

*Senior Research Engineer, Aerothermodynamics Branch; AIAA Fellow
†Assistant Branch Head, Aerothermodynamics Branch; AIAA Senior Member
‡Assistant Branch Head, Computational Aero Sciences Branch; AIAA Senior Member
§Aerothermodynamics Branch; AIAA Senior Member
¶Aerothermodynamics Branch; AIAA Senior Member
‖Aerothermodynamics Branch
**Computational Aero Sciences Branch
††Computational Aero Sciences Branch; AIAA Associate Fellow

expansions, and free shear layers in a hypersonic flow. Consequently, NASA has undertaken a program to develop and mature the speed and reliability of unstructured grid algorithm capabilities to a point where the analyses currently performed by LAURA and DPLR eventually can be replaced.

The unstructured grid code FUN3D has been modified to include the physical models used in LAURA for aerothermodynamic applications. Indeed, both codes share the exact same modules for thermodynamics, transport properties, chemical kinetics, thermal relaxation, and radiation. The "generic-gas path" through FUN3D has primarily tested a multi-dimensional reconstruction algorithm to address challenges associated with obtaining accurate heating on unstructured grids.[4,5] The generic-gas extension of FUN3D is now directed on maturing the test suites and user interfaces to enable it to replace LAURA for aerothermodynamic simulations, especially focussed on problems supporting Entry, Descent, and Landing (EDL) applications. A critical element of this extension is documentation of the functional equivalence of FUN3D to LAURA for EDL applications. The objective of this paper is to report on the progress of these functional equivalence tests. It will also describe algorithmic modifications required for a node-based unstructured grid code (FUN3D) to reproduce functionality of a cell-centered structured code (LAURA). Finally, it will briefly discuss new functional capabilities not currently in LAURA that are planned to enhance FUN3D's utility for EDL applications.

II. FUN3D and LAURA

FUN3D is a node based, fully unstructured, finite volume solver of the Euler and Navier-Stokes equations.[6] The baseline method uses Least Squares (LS) gradient information to execute second-order accurate inviscid flux reconstruction.[7] A Green-Gauss formulation of gradients at the nodes is used for multi-dimensional reconstruction. Viscous gradients across elements are also computed from a Green-Gauss formulation. A suite of modules includes all of the gas physics models in LAURA and Viscous Flow Algorithm for Complex Flow Analysis code (VULCAN)[8] for thermodynamics, transport properties, chemical kinetics, and thermal relaxation. The baseline inviscid flux reconstruction algorithms in the generic gas path mimic LAURA in that they utilize quasi-one-dimensional (edge-based) reconstruction using Roe's averaging[9] with Yee's symmetric total variation diminishing algorithm[10] adapted for unstructured grids.[5]

LAURA is a structured-grid, finite-volume solver, specialized for hypersonic re-entry physics.[1,11] Key elements of LAURA include Roe's averaging[9] and Yee's symmetric total variation diminishing (STVD) algorithm[10] for the formulation of second-order, inviscid flux. Yee's STVD formulation has been found to be exceptionally robust and Courant-number-independent using first point-implicit and then line-implicit relaxation for hypersonic flow simulations. The STVD algorithm uses a non-linear, min-mod function as a flux limiter that maintains second-order accuracy away from extrema but can admit limit cycles in the convergence process, particularly in the vicinity of captured shocks. This occurrence usually manifests itself as a stalling of convergence at a very low error norm, essentially a benign ringing in the solution at a level that has no impact on aerothermodynamic quantities. Viscous flux is computed using central differences.

Surface heating in FUN3D is captured from the integral conservation of flux through the dual control volume bounding the surface in the energy conservation law. That is, gradients of temperature and species concentration are directly calculated in the interior of the domain but not across the surface (as in LAURA). Rather, the net energy flux through the surface boundary must balance the inviscid and viscous flux across all other surfaces of the dual.

Eigenvalue limiting (Harten entropy fix[12]) is required by both LAURA and FUN3D to enable stable shock captures and prevent the formation the carbuncle phenomenon.[13,14] Implementation of limiting in both codes differs due to infrastructure.[5] In LAURA, it is known that surface heating can be augmented by application of eigenvalue limiting across the boundary-layer by as much as 20%. This problem is resolved by scaling back the magnitude of the limiter in the direction normal to the boundary layer for the linear waves. The unstructured formulation of FUN3D provides no information regarding the orientation of the dual control volume surfaces relative to the boundary layer or to the vehicle surface. A viscous switch in FUN3D rescales the limiter as a function of local cell Reynolds number. The cell Reynolds number uses a characteristic length across a face defined as the ratio of cell volume average across the face divided by face area. Impact of this limiting will be discussed after reviewing results of the functional equivalence test cases.

III. Functional Equivalence Overview

LAURA already uses a web-based regression test system that automatically checks for any impact of software changes to established functionality.[15] FUN3D uses these established tests (reported in Case A – Case O below) to confirm that its own functionality reproduces that of LAURA over a suite of test cases that touch most permutations of physical models, total energy, and geometric complexity of interest to EDL. These tests span perfect-gas, equilibrium, and thermochemical non-equilibrium gas chemistries representative of Earth, Martian, and Titan atmospheres. Axisymmetric and three-dimensional, blunt and slender configurations are included. In general, agreement with LAURA on identical grids and identical physical models is targeted to +/-4% for surface pressure and heating. In any cases where that target is missed additional analysis will be performed to explain the differences (i.e. grid convergence associated with node-based versus cell based algorithms or differences in the implementation of limiters required by the code infrastructure). Given that the purpose of this paper is to demonstrate functional equivalency between LAURA and FUN3D, only relative differences in results between the two codes will be shown without providing specific details about vehicle geometry or magnitudes of simulated environments.

Several capabilities in LAURA work flow have been reproduced in FUN3D to encourage users to make the transition.

1. A "shuffle" utility allows solution restarts from disparate physical models involving different numbers of governing equations. This capability, now available in FUN3D, utilizes a template in which new variables are initialized as needed, old variables are retained, and variables are eliminated if unused in the new model set. Examples include starting an 11-species air model from a 7-species air model solution or a two-equation turbulence case from a laminar case.

2. FUN3D has long had an algorithm for identifying lines of nodes off the body to enable line-implicit relaxation. This algorithm has been extended for prismatic grid systems spanning the entire shock layer to reproduce the quasi-one-dimensional grid adaptation in LAURA. The outer boundary may be aligned with the captured bow shock and the distribution of nodes in the boundary layer may target a user specified cell Reynolds number. This infrastructure has also enabled implementation of coupled radiation (Case M below) and algebraic turbulence models (Cases F and N below).

3. Ray tracing from any point on the surface in any direction through the shock layer is available in both LAURA and FUN3D to support analysis of uncoupled, three-dimensional radiative transport. The capability is required in situations where a tangent-slab approximation is not appropriate for analysis of radiative energy transfer to the surface. In the general case (not yet implemented) the algorithm must also be able to interpolate information from rays back to solution nodes to enable computation of coupled radiation – including the radiation source term in the energy equation.

All solutions are obtained on identical grids with provenance from the quasi-one-dimensional grid adaptation algorithm used in the LAURA solutions. These grids follow best practices in LAURA. In all cases, mesh spacing Δn at the wall on the forebody puts the cell Reynolds number in the range $0.1 \leq \rho_w c_w \Delta n/\mu_w \leq 2$ where

$$N_{cell} = \rho_w c_w \Delta n/\mu_w \tag{1}$$

and ρ_w, c_w, and μ_w are the density, speed of sound, and viscosity at the wall, respectively. Requirements for a grid-converged solution are problem dependent. Following LAURA best practices and based on previous grid convergence studies on closely related problems[16–22] we would expect a maximum change in surface heating distribution on the forebody of less than 8% (usually lower for attached flow).

Risk in the migration from LAURA to FUN3D has been mitigated through extensive re-use of modules currently in LAURA. Modest challenges associated with conversion of cell-based boundary conditions to node-based in FUN3D and with reformulation of limiters without dependence on structured-grid infrastructure are being addressed. The primary risk to full implementation derives from a continued requirement for high quality, semi-structured (prismatic) grids to achieve acceptable accuracy in simulation of heating in the presence of strong shocks. Offering options in multi-dimensional reconstruction to allow more extensive use of tetrahedral grids and developing options for grid alignment with shocks and/or bow shock fitting are mitigating this risk in FUN3D. Ultimately, if requirements for initial grid generation quality are not substantially relieved it will be more difficult to convince current users of LAURA and DPLR to switch.

IV. Functional Equivalence Tests

A. Case A: Sphere, Perfect Gas

Figure 1a compares the FUN3D solution for pressure p (black line) and laminar, convective heating q (red line) to the corresponding LAURA solution (bars). Axisymmetric flow conditions are for a standard, 5 km/s test case, discussed extensively in previous papers.[4,5] The ordinate of the figure uses a $\log_{10}$ scale so that the LAURA bars, scaled to ±4% of the LAURA solution, appear as a constant height in the figure. Pressures and heating predicted by both codes are in excellent agreement. A very slight bump in the heating distribution approaching the axis is evident in both solutions is an artifact of eigenvalue limiting to suppress a carbuncle.

(a) Case A, sphere

(b) Case B, spherically capped cone

Figure 1: Comparison of surface pressure and convective heating between simulations using LAURA and FUN3D for laminar, hypersonic flow of a perfect gas.

B. Case B: Spherically-Capped Cone, Perfect Gas

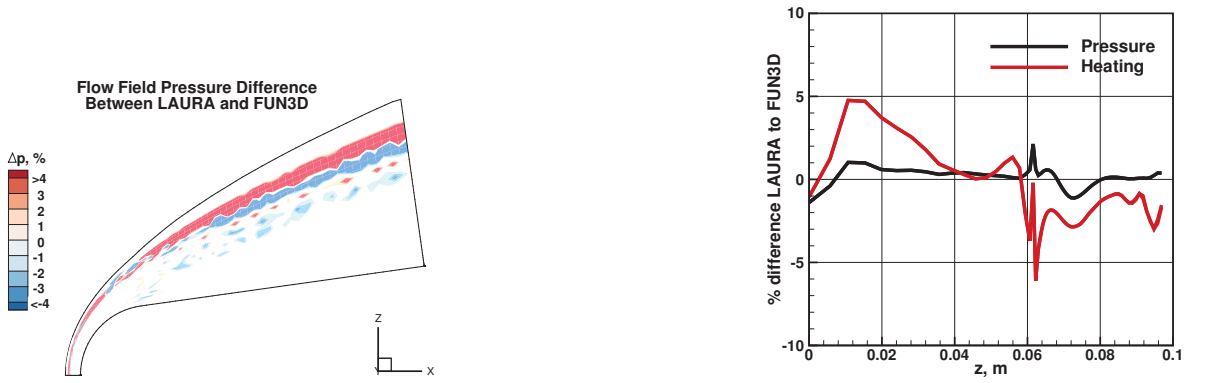

(a) Percent difference of pressure in symmetry plane.

(b) Percent difference of pressure and heating along the surface.

Figure 2: Additional functional equivalence metrics for Case B, a perfect gas, spherically capped cone simulation.

Similar to Case A, Fig. 1b again shows good agreement between FUN3D and LAURA for 1 km/s, laminar flow of a perfect gas over a spherically-capped cone. Figure 2 provides more detail of functional equivalence between the codes. Figure 2a shows that pressure differences are less than 4% across the symmetry plane except for slightly higher differences across the captured shock. Figure 2b shows a heating difference as large as 5% in the stagnation region and at the sphere-cone junction. These differences are likely associated with node-centered (FUN3D) versus cell-centered (LAURA) formulations of the discretization and heating is especially sensitive to such differences.

C. Case C: Sphere, Air, Thermochemical Nonequilibrium

This case reprises the conditions of Case A for a 5-species air model in thermochemical non-equilibrium (two-temperature model).[11] A radiative equilibrium, super-catalytic wall boundary condition (all species catalyzed to their respective values of mass fraction in the free stream) is applied with emissivity of 0.89. A wall temperature update factor of 0.05 was sufficient to maintain stability.

Figure 3 compares the FUN3D solution for pressure p (black line) and laminar, convective heating q (red line) to the corresponding LAURA solution (bars). Recall, the ordinate of the figure uses a $\log_{10}$ scale so that the LAURA bars, scaled to $\pm 4\%$ of the LAURA solution, appear as a constant height in the figure. Pressures are in excellent agreement. The FUN3D solution skirts just above the 4% bar relative to LAURA in the stagnation region – a trend that repeats in other non-perfect-gas cases to follow.

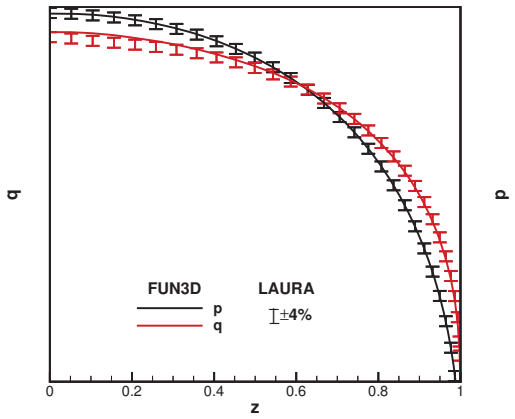

Figure 3: Comparison of surface pressure and convective heating between simulations using LAURA and FUN3D for laminar, hypersonic flow of 5-species air in thermal non-equilibrium.

D. Case D: Capsule, Axisymmetric, Laminar Flow, Perfect Gas

Entry, descent, and landing vehicles often utilize capsule shapes composed of a spherical segment with a circular shoulder transitioning to an after body containing the payload. Spherical segment shapes tend to be very blunt and they accentuate potential problems associated with carbuncle formation simply because the percentage of the shock layer characterized by small eigenvalues is increased. Larger regions of near-stagnation conditions are more challenging to compute.

Figure 4 compares the FUN3D solution for pressure p (black line) and laminar, convective heating q (red line) to the corresponding LAURA solution (bars). The flatter profiles of pressure and heating approaching the axis ($z = 0$) are indicative of the broader stagnation region across the spherical segment. The FUN3D surface pressures are with 4% of the LAURA values at every node except on the shoulder, and heating lies along the upper boundary of the LAURA 4% bar. Heating and pressure around the shoulder (approaching $z = 2$) is offset by larger amounts; however, this difference is easily interpreted as interpolation errors between the node-based and cell-based solutions across a rapidly varying function.

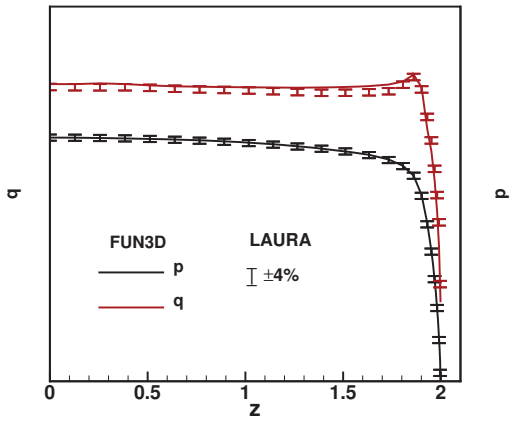

Figure 4: Comparison of surface pressure and convective heating between simulations using LAURA and FUN3D for laminar, hypersonic (Mach 6), perfect-gas flow over a capsule-like geometry.

E. Case E: Capsule, 3D, Laminar Flow, N_2 as Perfect Gas

This case simulates a laminar, Mach 8 wind tunnel flow over a capsule shape in nitrogen modeled as a perfect gas. Like the previous case, it involves flow over a capsule-like geometry but at angle-of-attack α of 28 degrees. Figure 5(a) compares the FUN3D solution for pressure p (black line) and laminar, convective heating q (red line) to the corresponding LAURA solution (bars) on a cut orthogonal to the symmetry place at the axis to the shoulder. Figure 5(b) presents the same relative differences along the symmetry plane on the surface. Figure 5(c) provides a contour of relative differences on a color scale that emphasizes locations where FUN3D is more than 4% larger than LAURA (dark red) or more than 4% lower than LAURA (dark blue). All three plots show excellent agreement with pressure. FUN3D tracks slightly higher than 4% of LAURA for heating over acreage on the upper half of Fig. 5(c) – the region farthest from the stagnation point near the lower edge of this figure.

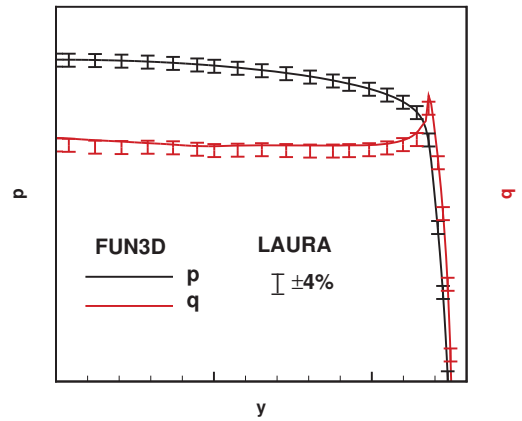

(a) Laminar flow. Planar cut through axis, orthogonal to symmetry plane.

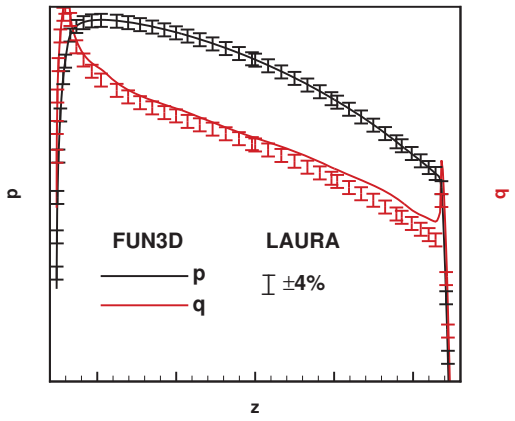

(b) Laminar flow. Symmetry plane cut.

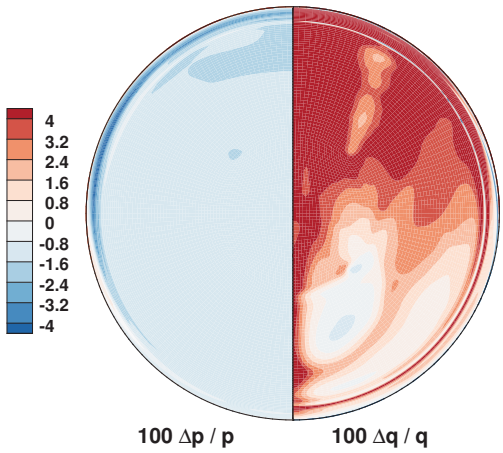

(c) Global view of relative differences in pressure (left) and heating (right) for laminar flow.

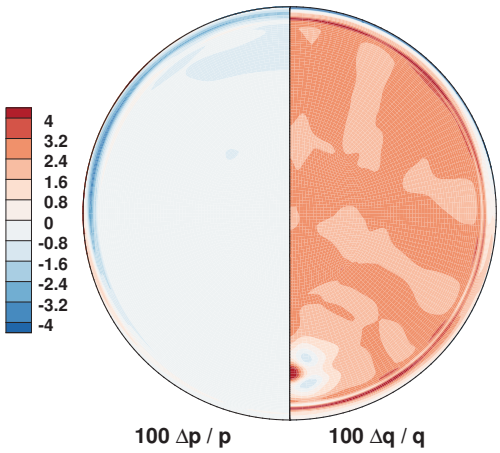

(d) Global view of relative differences in pressure (left) and heating (right) for turbulent flow.

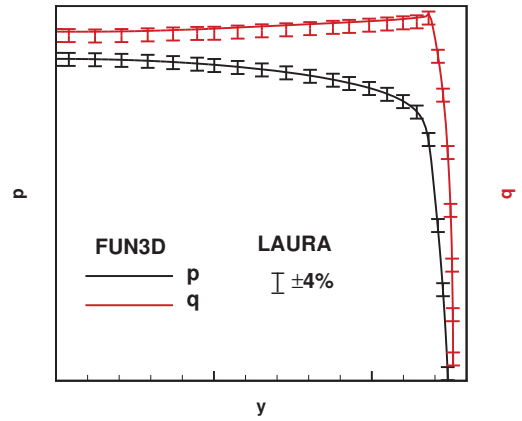

(e) Turbulent flow. Planar cut through axis, orthogonal to symmetry plane.

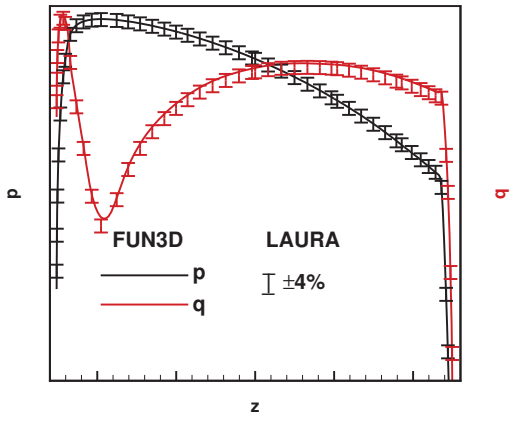

(f) Turbulent flow. Symmetry plane cut.

Figure 5: Comparison of surface pressure and convective heating between simulations using LAURA and FUN3D for hypersonic (Mach 8), perfect-gas flow over a capsule-like geometry at $\alpha = 28$.

F. Case F: Capsule, 3D, Turbulent Flow, N_2 as Perfect Gas

This case repeats conditions of the previous case E but models turbulent flow with the algebraic Cebeci-Smith[23,24] turbulence model. Figure 5(e) compares the FUN3D solution for pressure p (black line) and laminar, convective heating q (red line) to the corresponding LAURA solution (bars) on a cut orthogonal to the symmetry place at the axis to the shoulder. Figure 5(f) presents the same relative differences along the symmetry plane on the surface. Figure 5(d) provides a contour of relative differences on a color scale that emphasizes locations where FUN3D is more than 4% larger than LAURA (dark red) or more than 4% lower than LAURA (dark blue). All three plots again show excellent agreement with pressure. FUN3D heating is in better agreement with LAURA for the turbulent simulation though it still tends to run at the high end of the 4% band. The red dot at the stagnation point of Fig. 5(d) suggests that differences in the eigenvalue limiting algorithm have a stronger effect on the heating than elsewhere on the surface.

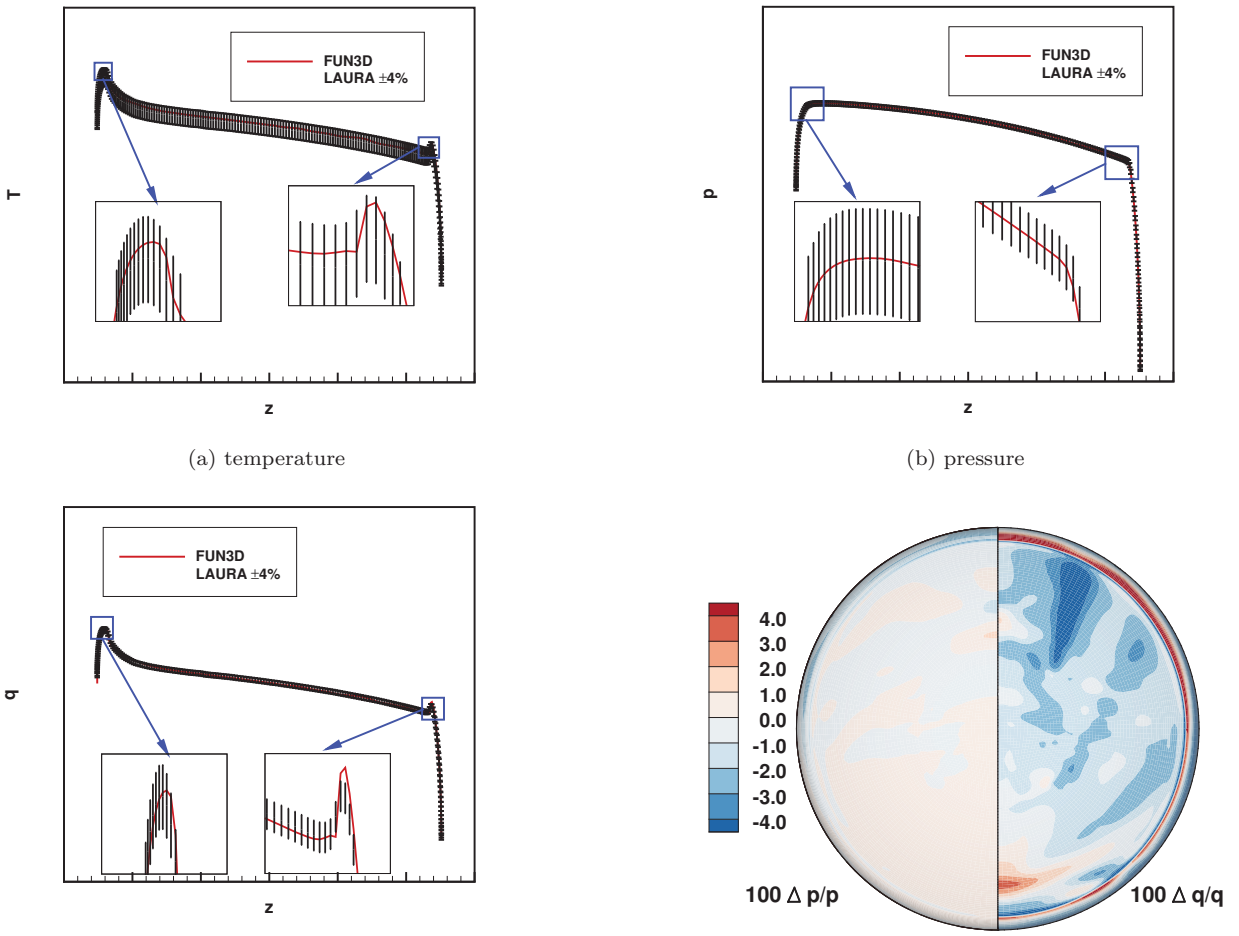

(a) temperature

(b) pressure

(c) heating

(d) Contour plot of relative difference in pressure and heating between LAURA and FUN3D.

Figure 6: Comparison of surface pressure and heating between simulations using LAURA and FUN3D for hypersonic (6.35 km/s) flow of 5-species air in chemical nonequilibrium over a capsule geometry at $\alpha = 28$.

G. Case G: Capsule, 3D, Laminar Flow, 5-Species

This case (Fig. 6) simulates hypersonic flow ($V_\infty = 6.35$km/s) over a capsule in 5-species air in chemical non-equilibrium at angle-of-attack α of 28 degrees. Species mass fractions at the wall are computed assuming a super-catalytic boundary condition. A radiative equilibrium wall temperature boundary is assumed. Line cuts along the symmetry plane in Fig. 6(a-c) for temperature, pressure, and heating generally show good agreement (within 4%) between FUN3D and LAURA. Details of the comparisons at the shoulders shown in

each figure indicate a slightly larger prediction of heating by FUN3D repeating the observation first made in case D and also evident in cases E and F. Figure 6(d) provides a contour of relative differences on a color scale that emphasizes locations where FUN3D is more than 4% larger than LAURA (dark red) or more than 4% lower than LAURA (dark blue) indicating excellent agreement with pressure (left side) and good agreement with heating (within 4% over most of the vehicle). A red ellipse at the stagnation point is again evident, indicating differences in the eigenvalue limiting algorithm as noted previously in case F.

H. Case H: Axisymmetric, Equilibrium flow by Free-Energy Minimization

This case reprises the conditions of Case C for a 5-species air model in chemical equilibrium as computed by free-energy minimization.[25] A constant wall temperature (T_w = 500K) and super-catalytic wall boundary condition are applied. Good agreement is evident between LAURA and FUN3D for pressure and heating in Fig. 7(a). Comparison of pressure and temperature in the symmetry plane (Fig. 7(b)) indicate small differences associated with the shock capturing. Pressure near the outflow boundary in FUN3D is approximately 4% lower than in LAURA – an explanation for this difference is not yet evident and was not seen earlier in Fig. 2(a). The root mean square of differences across the shock layer is 1.53% for pressure and 0.48% for temperature.

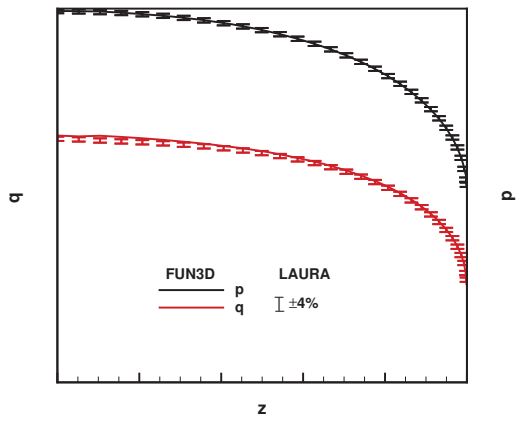

(a) Percent difference of pressure and heating along the surface.

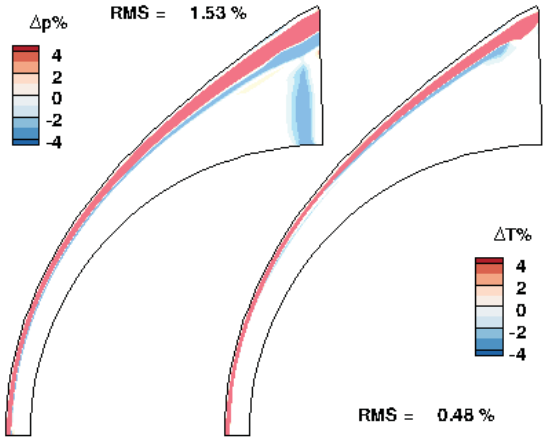

(b) Percent difference of pressure and temperature in the symmetry plane.

Figure 7: Comparison of pressure, temperature, and heating between simulations using LAURA and FUN3D for laminar, hypersonic flow of 5-species air in chemical equilibrium as computed by free-energy minimization.

I. Case I: Space Shuttle Orbiter, Finite-Catalytic Wall

LAURA solutions of hypersonic flow over the Shuttle Orbiter have been reported previously.[26–28] Comparisons of FUN3D with LAURA for this application have also been presented.[5] The comparisons are repeated here at Mach 23 in a manner consistent with the metric requirements for these functional equivalency tests. This case is the first to test a finite-catalytic wall boundary condition[29] and to test significant vortical separation to the lee side of a winged vehicle.

Comparisons of pressure and heating from LAURA and FUN3D on cuts along the symmetry plane, chord wise across the wing, and circumferentially across the wing–body are presented in Fig. 8. The upper leg of the curve in these figures show conditions on the wind side of the surface cut, where pressures and heating are higher than on the lee side of the vehicle. One exception to this trend is in Fig. 8(b) where heating on the leading edge of the vertical tail shows relatively higher magnitude. The wind side surface comparisons are generally within the 4% band. The lee side comparisons show significant excursions outside the 4% band in both pressure and heating. These lee side excursions in heating are relatively small in absolute magnitude. They appear to be in regions where previously separated flow washes over a surface and may include integrated effects of algorithm differences on a node distribution that is not grid converged. Some differences are caused by a modified outflow boundary to prevent reverse flow off the lee side wing trailing edge.

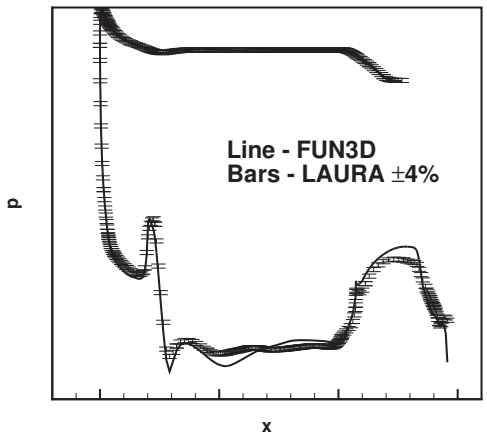

(a) Symmetry plane cut - pressure.

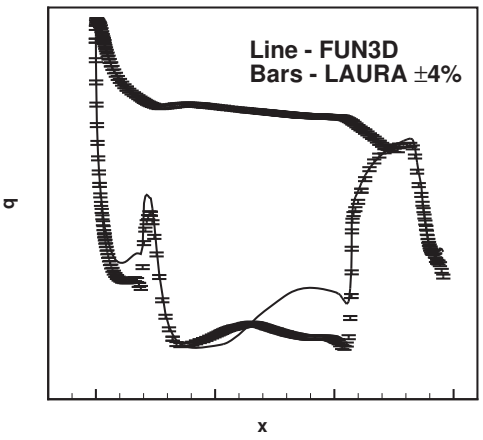

(b) Symmetry plane cut - heating.

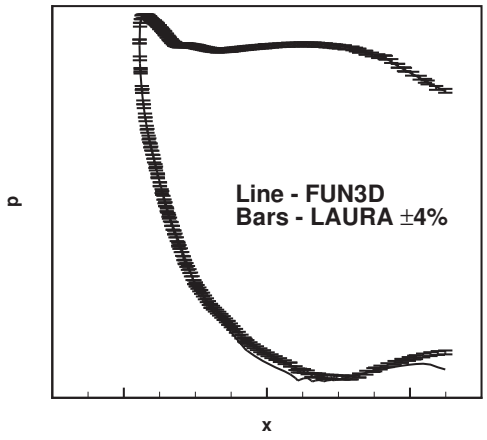

(c) Chordwise cut across wing - pressure.

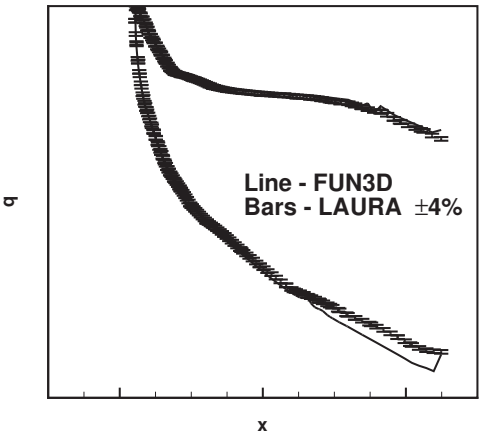

(d) Chordwise cut across wing - heating.

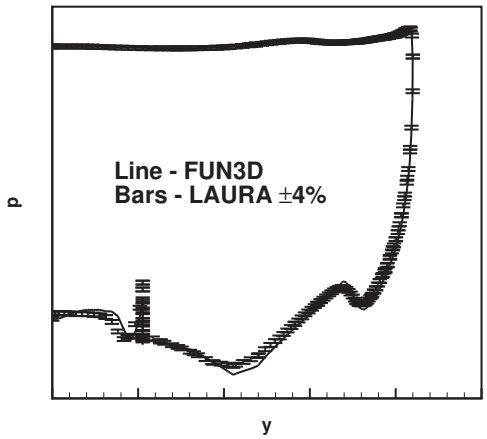

(e) Circumferential cut across wing-body - pressure.

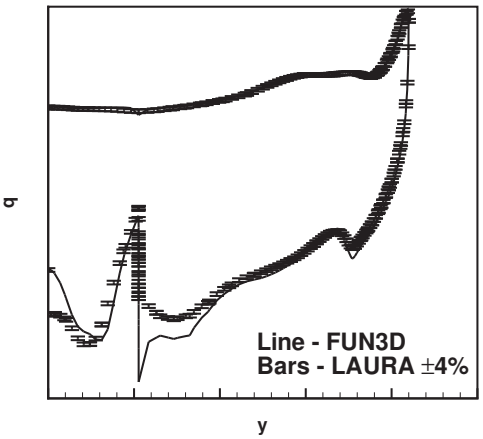

(f) Circumferential cut across wing-body - pressure.

Figure 8: Comparison of surface pressure and heating between simulations using LAURA and FUN3D for hypersonic (M = 23), flow of 5-species air in chemical nonequilibrium over a Shuttle Orbiter geometry at $\alpha = 40$.

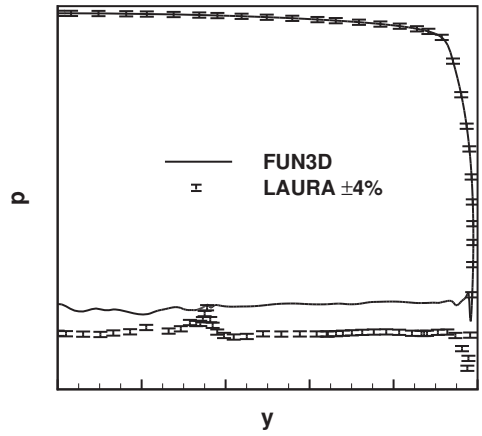

(a) Planar cut through axis, orthogonal to symmetry plane - pressure.

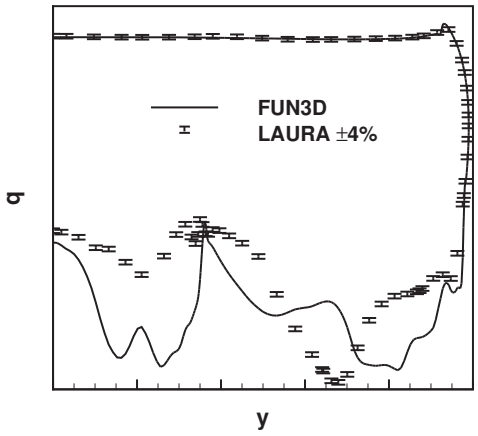

(b) Planar cut through axis, orthogonal to symmetry plane - heating.

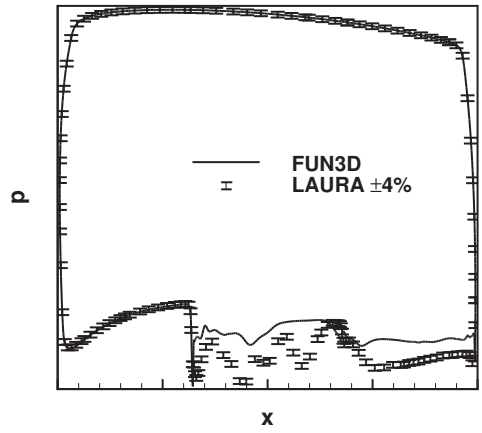

(c) Symmetry plane cut - pressure.

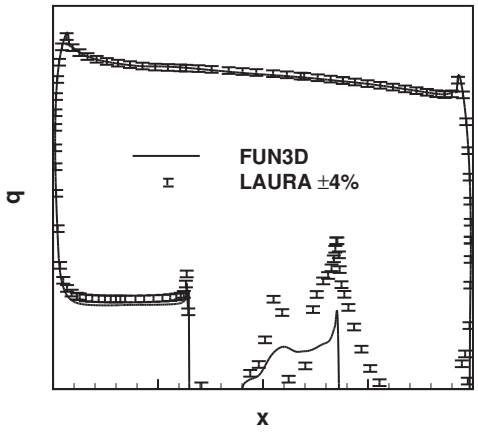

(d) Symmetry plane cut - heating.

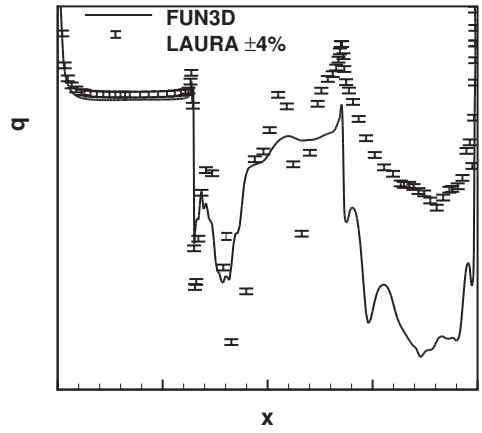

(e) Symmetry plane cut - wake heating detail.

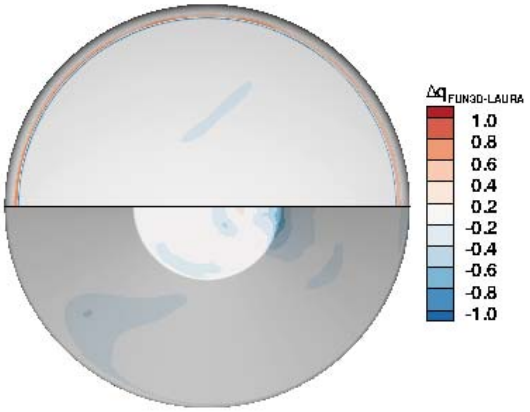

(f) Heating difference. Top - windside. Bottom - leeside.

Figure 9: Comparison of surface pressure and heating between simulations using LAURA and FUN3D for hypersonic (M = 10, 3.3 km/s), flow of 5-species air in chemical nonequilibrium over a capsule geometry at $\alpha = 28$.

J. Case J: Capsule Including Wake Flow

This case is the first to feature near wake flow behind a capsule shape including effects of gas chemistry at Mach 10, $V_\infty = 3.3$km/s. Boundary conditions include a super-catalytic wall and radiative equilibrium wall temperatures. Figure 9(a-e) compares pressure and heating between LAURA and FUN3D along planar cuts that are orthogonal to or aligned with the symmetry plane. The upper leg of the curves indicate conditions on the wind side surface and the lower leg of the curves capture the lee side surface conditions. Both pressure and heating are within the 4% band on the wind side (recall the bar height is ± 4% of LAURA and the bar height is constant using a logarithmic ordinate). There are significant excursions on the lee side; Fig. 9(e) is a rescaled version of Fig. 9(d) to highlight these differences. As with the lee-side surface comparisons of the previous Shuttle Orbiter case it appears that the integrated effects of algorithm differences in regions where the separated flow may not be grid converged are the likely cause of the excursion. Consider, for example, the good agreement evident in the lower left hand corner of Figs. 9(c-d) (upper left hand corner of rescaled Fig. 9(e)). This good agreement occurs on the lee side surface where the flow remains attached. It is not until the flow separates, and the surface is bathed in flow that has previously separated elsewhere, that the differences significantly exceed 4%. At this point it is not known if the failure to achieve grid convergence is an issue in only LAURA or only in FUN3D or in both codes. While these percent differences are large Fig. 9(f) shows that the magnitude of the differences between LAURA and FUN3D are everywhere less than 1 W/cm^2 on the fore body (top half of figure) and aft body (bottom half of figure).

K. Case K: CO_2

The results of Fig. 10 show good comparisons with pressure and heating for a case designed to bring in Martian atmosphere properties into the test suite. This single species CO_2, thermal equilibrium case does not significantly stress the test suite except for the variation of heat capacity of a linear, triatomic molecule. More complex chemical models are planned relevant to the Martian atmosphere in the future.

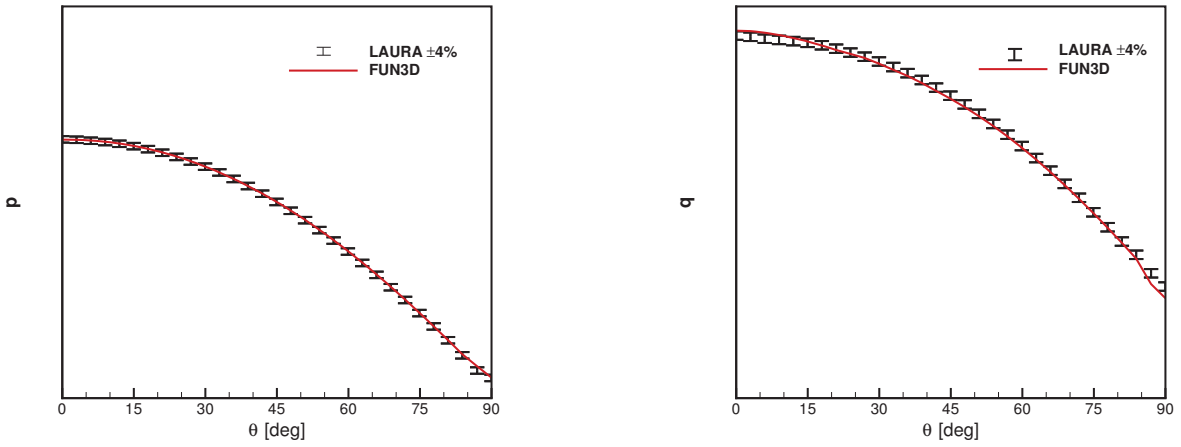

(a) pressure

(b) heating

Figure 10: Comparison of surface pressure and heating between simulations using LAURA and FUN3D for Mach 6.2 (2.8 km/s), flow of single species CO_2 over a sphere.

L. Case L: Titan Entry, 18-Species, Thermochemical Nonequilibrium

In contrast to the simplicity of the chemical model of Case K, the present case tests an 18-species thermochemical nonequilibrium model for the entry of a 70 degree spherically capped cone into the atmosphere of Titan. The atmospheric model assumes 0.9708 N_2 and 0.0292 CH_4 by mass in the free stream. Remaining species include: N, C, H, CH_3, CH_2, CH, H_2, C_2, NH, CN, Ar, H^+, N^+, Ar^+, N_2^+, and e^-. This is the first test in the suite to include charged particles in the model. Boundary conditions include a super-catalytic wall and radiative equilibrium wall temperatures. The simulation is for a trajectory point in the Titan entry of Mach 22.6 (5.761 km/s). Axisymmetric flow is assumed. Comparisons of pressure and heating in Fig. 11 indicate that FUN3D is within the 4% band of LAURA.

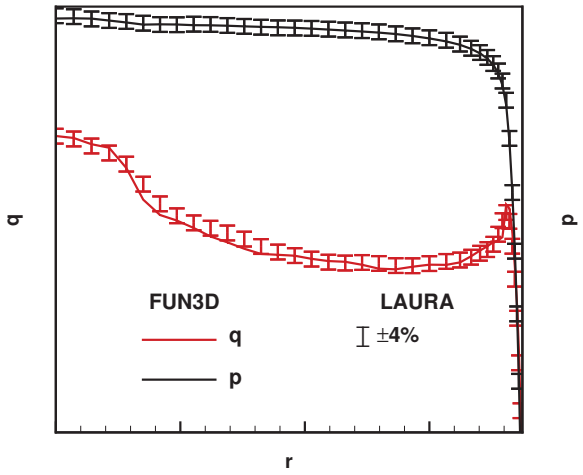

Figure 11: Comparison of surface pressure and heating between simulations using LAURA and FUN3D for Mach 22.6 (5.761 km/s), flow of 18-species nitrogen-methane mixture over a 70 degree spherically-capped cone.

M. Case M: Coupled Radiation, 11-species Air, Thermochemical Nonequilibrium

A simulation including fully coupled radiative heating at the FIRE II[30,31] 1643 second trajectory point (V_∞ = 10.84 km/s and ρ_∞ = 0.00078 kg/m^3) is presented in Fig. 12.[32] Both simulations used the HARA radiation code[16] and an 11-species, two-temperature thermochemical non-equilibrium gas model. Agreement between the two codes for convective and radiative heating is generally good. This routine uses the line extraction capability described in the previous section to transfer radiative flux information between FUN3D and HARA assuming the tangent-slab approximation. Matching the radiative heating is simply a confirmation that the profiles of species densities and vibrational-electronic temperatures being passed to HARA from LAURA and FUN3D are in good agreement.

N. Case N: Multi-component Diffusion with Stefan-Maxwell Equations

The tests in this case engage two new capabilities. The first is multi-component diffusion through a sub-iteration of the Stefan Maxwell equations.[33] The second is imposition of an equilibrium catalytic boundary condition where species mole fractions at the wall are determined a s a function of wall pressure, temperature, and elemental mass fractions diffusing to the wall.[25] Simulated conditions are for Mach 25 flow (8 km/s) of 11-species air in thermochemical nonequilibrium. Comparison of pressure and heating between LAURA and FUN3D are presented in Fig. 13 for laminar flow and turbulent flow using the Cebeci-Smith algebraic turbulence model.[23] Pressures are in excellent agreement. The heating in both the laminar and turbulent models skirt the upper limit of the 4% band, indicating possible effects of the eigenvalue limiting routine differences in the stagnation region.

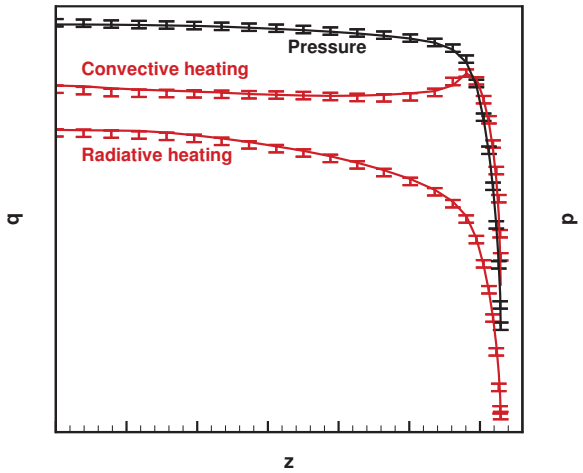

Figure 12: Comparison of convective and radiative heating between simulations using LAURA and FUN3D for FIRE II case at 1643 sec. Lines are FUN3D. Bars are ± 4% of LAURA.

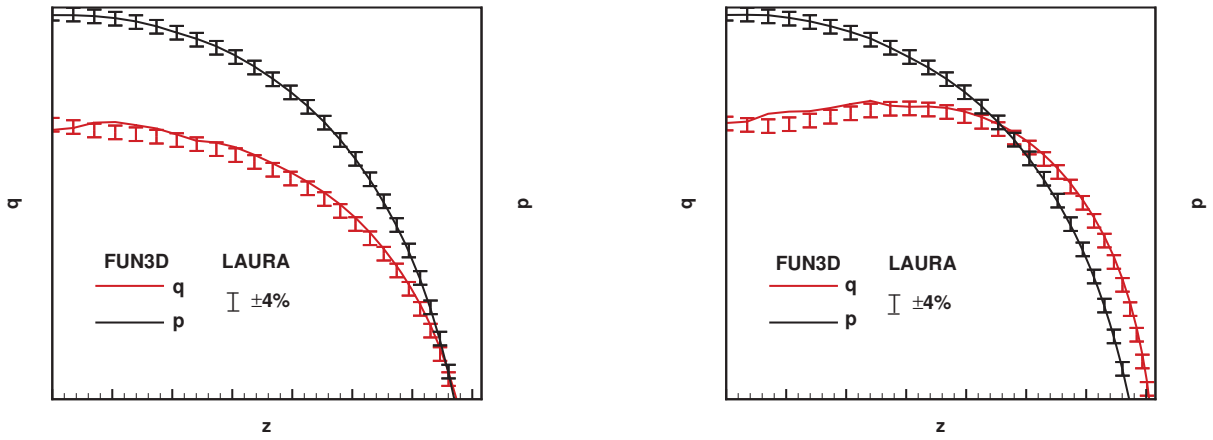

(a) Laminar

(b) Turbulent (Cebeci-Smith)

Figure 13: Comparison of surface pressure and heating between simulations using LAURA and FUN3D for Mach 25 (8 km/s) flow of 11-species air over a sphere assuming multi-component diffusion using the Stefan Maxwell equations.

O. Case O: Compression Ramp, Two-Equation Turbulence Model

Hypersonic, turbulent flow over a 36 deg. ramp at Mach 11.3 (1.769 km/s) is modeled using the Wilcox 2006 k-ω two-equation turbulence model.[34] This case corresponds to Run 54 from CUBRC[35] and was thoroughly studied in a recent paper to quantify simulation uncertainty of shock wave – turbulent boundary layer interactions.[36]

Comparisons of pressure and heating are presented in Fig. 14. The pressure distributions are in good agreement (within 4%) starting from the strong interaction at the leading edge of the plate at the left through the abrupt rise of pressure at the ramp and the post interaction at the right. However, heating from FUN3D coming off the strong interaction and post-shock interaction is in poor agreement with the LAURA baseline and further analysis of the multi-equation turbulence models are required.

Recall that the intent of these comparisons is to confirm that, given the same set of physical models, both codes give the same result within uncertainty introduced by grid convergence. The accuracy of the simulation relative to real physics as determined by experimental measurements with associated measurement error is not identifiable in this comparison. Indeed, the CUBRC data and other models show a greater extent of separation in front of the ramp than shown in Fig. 14. A compressibility correction is required with this model to match the extent of separation.[36]

V. Eigenvalue Limiting

The sensitivity of stagnation region heating on the magnitude of eigenvalue limiting for case B is demonstrated in Fig. 15. The ordinate z defines radial distance from the stagnation point for the axisymmetric cone. The abcissa q is the heating magnitude for this perfect-gas case. The combination of line style and overlayed symbol shape defines the magnitude of the eigenvalue limiter in the following equations.

A maximum wave speed is defined

$$\lambda_{max} = \max\left(|U|, |V|\right) + c \tag{2}$$

where U, V are velocity components normal and tangent to the cell wall and c is the sound speed. Coefficients to limit the eigenvalues are defined

$$e_a \quad = \quad \max\left[0.01, \quad \min\left(1, \lambda_{a,lim}(1 - s(N_{cell}))\right)\right] \tag{3}$$

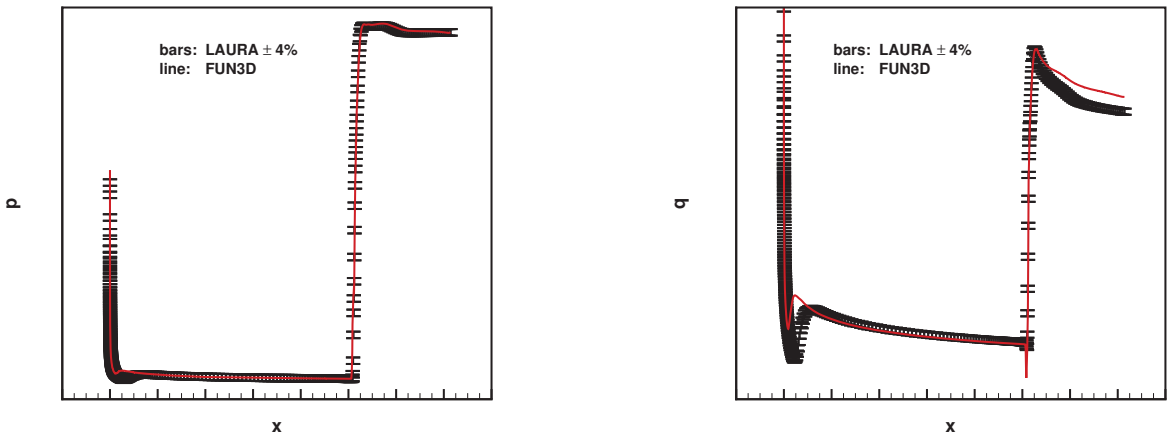

(a) Pressure

(b) Heating

Figure 14: Comparison of surface pressure and heating between simulations using LAURA and FUN3D for Mach 11.3 (1.769 km/s) flow of air modeled as a perfect gas over a 36 deg. ramp.

$$e_c \quad = \quad \max\left[0.00001, \min\left(1, \lambda_{c,lim}(1 - s(N_{cell}))\right)\right] \tag{4}$$

where N_{cell} is the cell Reynolds number (see Eq. (1)) and $\lambda_{a,lim}$ and $\lambda_{c,lim}$ are user defined limiting coefficients. These coefficients are identical in the present work and their values are denoted λ in the line style legend of Fig. 15. The function $s(N_{cell})$ in Eq. (5) is designed to drive the limiting coefficients e_a and e_c to a minimum value if $N_{cell} < \lambda_{L,1}$ and to its maximum value if $N_{cell} > \lambda_{L,2}$.

$$s(N_{cell}) = 1 - \max\left[0, \min\left(1, (N_{cell} - \lambda_{L,1})/(\lambda_{L,2} - \lambda_{L,1})\right)\right]^4 \tag{5}$$

The bounds on N_{cell} are denoted by the ordered pair λ_L in the symbol legend of Fig. 15. It is assumed that the user has some knowledge of how the grid spacing at the wall was defined and is able to set $\lambda_{L,1}$ and $\lambda_{L,2}$ so that the limiting may be substantially removed near the wall but retained in the upper portions of the boundary layer. If limiting is scaled back too much a pre-carbuncle reverse flow in the nodes near the wall is evident and a dip in the stagnation region heating is observed. The formulation of the limiting is completed as defined in Eqs. (6 - 9).

$$\lambda_a \quad = \quad e_a \lambda_{max} \tag{6}$$

$$\lambda_c \quad = \quad e_c \lambda_{max} \tag{7}$$

$$|U|_{lim} \quad = \quad \max\left[\lambda_c, \frac{1}{2}\left(\frac{U^2}{\lambda_c} + \lambda_c\right)\right] \tag{8}$$

$$|U \pm c|_{lim} \quad = \quad \max\left[\lambda_a, \frac{1}{2}\left(\frac{(U \pm c)^2}{\lambda_a} + \lambda_a\right)\right] \tag{9}$$

For any ordered pair of limiting coefficients on cell Reynolds number $\lambda_{L,1}$ and $\lambda_{L,2}$ it is noted that the effect of increasing limiting coefficient on the maximum wave speed λ is to increase stagnation point heating – consistent with LAURA behavior. The effect of the limiter away from the stagnation point (larger z) begins to diminish – mainly because the $|U|$ is itself larger and not modified by the limiting. (If the body is blunter then the magnitude of $|U|$ remains small over a greater domain and more affect may be expected.) A setting with $\lambda = 0.6$ (the red lines in Fig. 15) is most consistent with default settings in LAURA.

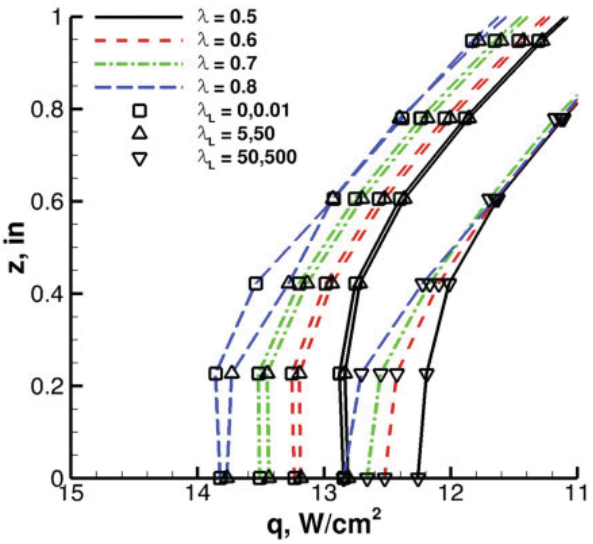

Figure 15: Sensitivity of stagnation region heating to numerical parameters.

The sensitivity of heating to the limiting based on N_{cell} is much less than observed in LAURA (possibly due to the integral formulation of surface heating discussed previously in Sec. II. The first ordered-pair for $\lambda_L = (0, 0.1)$ (square symbols) does not engage for the given grid with $N_{cell} > 0.1$. The second ordered-pair for $\lambda_L = (5, 50)$ (delta symbols) engages over the lower portion of the boundary layer but produces very little affect on heating magnitude. It is not until the third ordered-pair is engaged with $\lambda_L = (50, 500)$ (gradient symbols) that limiting is substantially removed across the domain and an abrupt lowering of heating is produced consistent with pre-carbuncle behavior.

In the tests documented herein eigenvalue limiting settings were chosen in an attempt to minimize the effects of limiting without allowing pre-carbuncle heating dips in the stagnation region. On average, it is observed that FUN3D solutions for heating tend to run on the high side of the 4% band of the LAURA baseline for attached flow. Excursions can be larger for separated flow cases I, J, O. The extent to which these larger differences are due to differences in the integrated effect of limiting across the separated shear layer or simply due to grid convergence issues is not known. More work is planned to better understand these issues and ultimately automate the selection of limiting parameters in this Roe/STVD based algorithm and to engage other flux function formulations in the generic gas path of FUN3D.

VI. Run Times

A representative time comparison between the two codes is provided in Fig. 16 associated with case H. The ordinate in these figures shows the convergence criteria – the percent change in stagnation point heating after 1000 relaxation steps. The abcissa documents the number of relaxation steps. Each solution started from the same cold start (uniform flow) on the same grid and ended when the change in stagnation point heating was less than 0.1%. The machine being used is a desktop workstation (server) with two Xeon 5640 quad-core processors and 48GB of memory. FUN3D and LAURA were compiled with Intel FORTRAN compiler version 12.x for mpi. Six processors were used for both the FUN3D and LAURA solutions. The FUN3D time, shown in red, is 472 seconds using a constant Courant number of 5. The LAURA solution, run with a default Courant number of 10^6, shows point-implicit relaxation times in Fig. 16(a) to convergence and switching to line-implicit relaxation after 6000 steps in Fig. 16(b). In the first case, LAURA requires 449 seconds and in the second case LAURA requires only 117 seconds to execute fewer, more efficient and more costly line relaxation steps.

Inherent differences in algorithm infrastructure make comparisons on equal footing difficult. In this axisymmetric case with identical grids, LAURA solves only 64x1x30 cells and FUN3D solves 65x2x31 nodes. Both codes freeze Jacobian updates for ten relaxation steps. LAURA updates the transport properties every

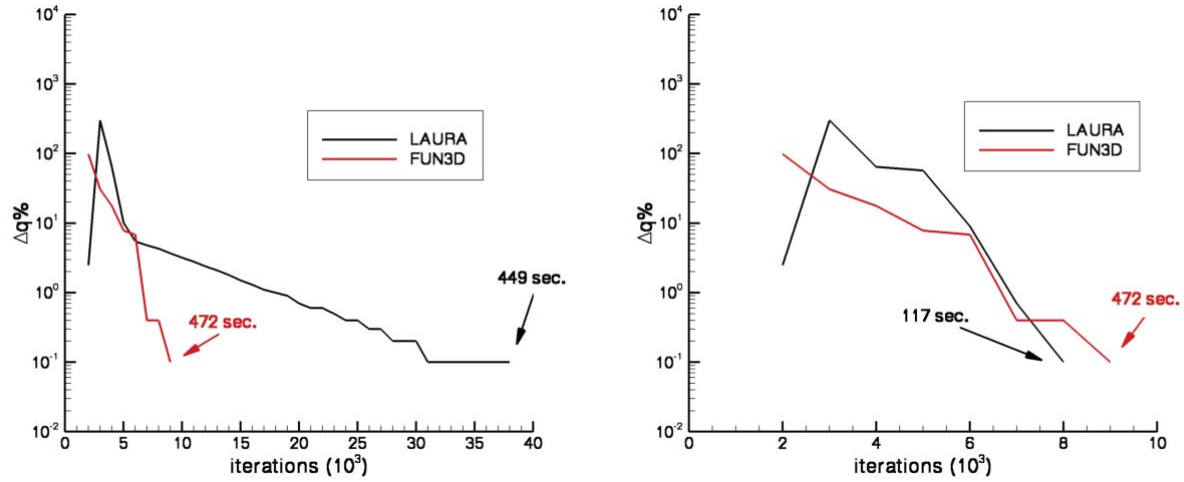

(a) LAURA point-implicit

(b) LAURA point- and line-implicit

Figure 16: Timing comparisons.

five steps but FUN3D updates them every relaxation step. It is observed that multi-species cases do not converge as efficiently as perfect-gas cases in FUN3D; consequently, it is suspected that the current implicit formulation of the multi-species surface boundary condition may impact efficiency of each relaxation step.

VII. Multi-Dimensional Reconstruction

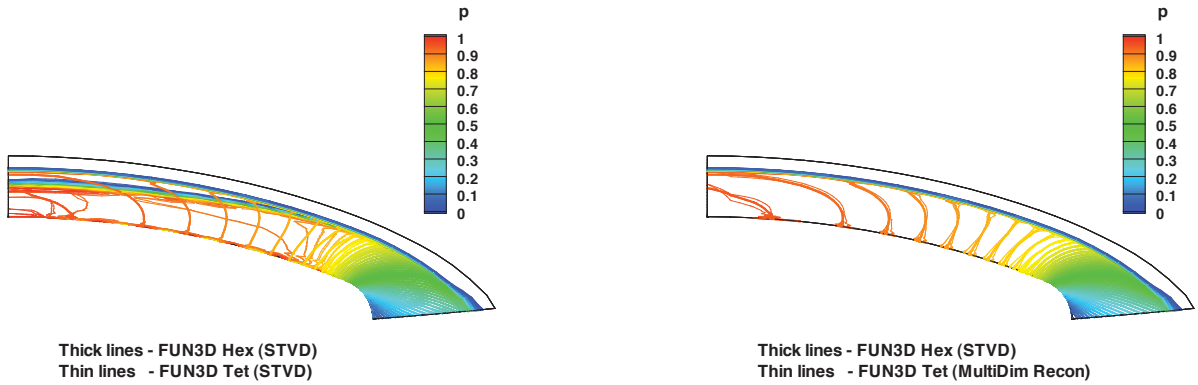

(a) Edge-based reconstruction on a tetrahedral grid.

(b) Multi-dimensional reconstruction on tetrahedral grid.

Figure 17: Pressure distribution in the plane of symmetry for uncoupled radiation simulation for Fire II on tetrahedral grid compared to hexahedral grid simulation.

A simulation related the Fire II test case M, without radiation, highlights some of the algorithmic issues related to hypersonic simulation on tetrahedral grids. Comparisons in the symmetry plane for pressure and temperature distributions made by FUN3D on tetrahedral and hexahedral grids and using edge-based reconstruction and multi-dimensional reconstruction are presented in Figs. 17 and 18. In this case, it is noted that a multi-dimensional reconstruction algorithm[5] is required when using tetrahedral grids with a symmetric, total-variation diminishing (STVD) formulation. In all cases, the hexahedral grid simulation provides simulation quality that is closest to LAURA (not shown here). Nevertheless, it is important to provide evidence of simulation quality on tetrahedral grids, as shown here, because grid generation and adaptation is most readily implemented on mixed element grid systems including tetrahedra. The importance

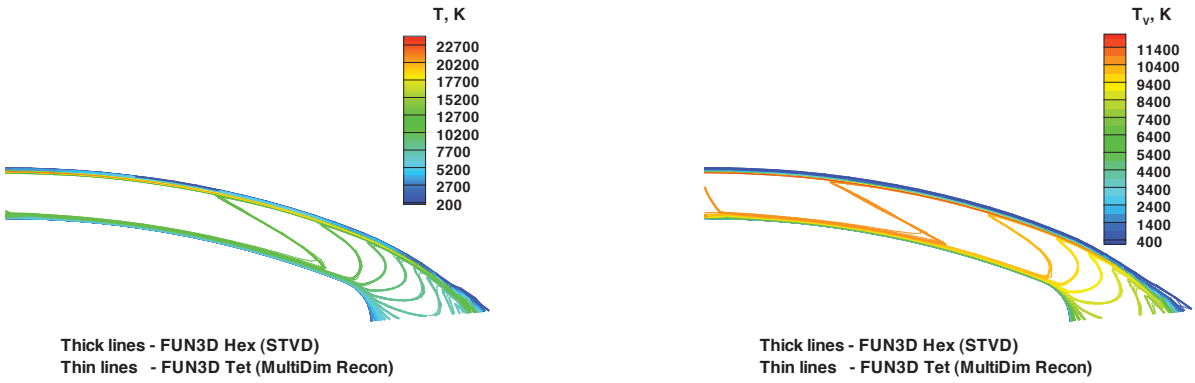

(a) Translational-rotational temperature.

(b) Vibrational-electronic temperature

Figure 18: Temperature distribution in the plane of symmetry for uncoupled radiation simulation for Fire II on hexahedral and tetrahedral grids.

of multi-dimensional reconstruction on heating has been reported previously.[5] The large scale effect on the shock layer evident in Fig. 17(a) is highlighted again here to give example of issues motivating future work on shock fitting and reconstruction with basis functions discussed in the next section.

VIII. Future Work

As of this writing there are four function capabilities in LAURA that are not yet in FUN3D. These include:

1. RCS jet inflow boundary condition – a boundary feeding a nozzle geometry for which plenum pressure and temperature are specified and inflow conditions through the boundary are calculated. This capability is scheduled for completion prior to October 2013.

2. Coupled Ablation – a boundary condition in which equilibrium steady state ablation may be assumed and ablation rate and species densities at the wall are calculated. This capability is scheduled for completion prior to October 2013. More comprehensive coupled ablation with material response codes are also being worked in LAURA and plans call for such coupling to be introduced to FUN3D in fiscal year 2014.

3. Micro-aerothermodynamic morphing – First introduced in the X-33 program and later used extensively to model Shuttle Orbiter thermal protection system damage,[28] the morphing capability enables a converged flow simulation over a smooth outer mold line to be captured and provide boundary conditions for subsequent aerothermal analysis of flow over a new geometry morphed from the original surface. Unstructured grids in FUN3D are more adaptable to morphed surfaces but at present there is no utility to capture an existing solution and re-run only the domain around the perturbation.

4. Grid sequencing with moving shock

New capabilities (not currently in LAURA but under development for FUN3D) include bow-shock-fitting and the use of orthonormal basis functions for multi-dimensional reconstruction.

A. Bow-shock-fitting

A shock fitting methodology is being implemented in FUN3D. The initial implementation will be restricted to fitting the free stream boundary to the bow shock. This will greatly alleviate the adverse effects associated with capturing the bow shock on unstructured grids. The node based unstructured grid implementation will involve using a steady state shock fitting method similar to that described by of Bonfiglioli[37] which uses the Rankine-Hugoniot relations to solve for the jump conditions thereby yielding the post shock state variables

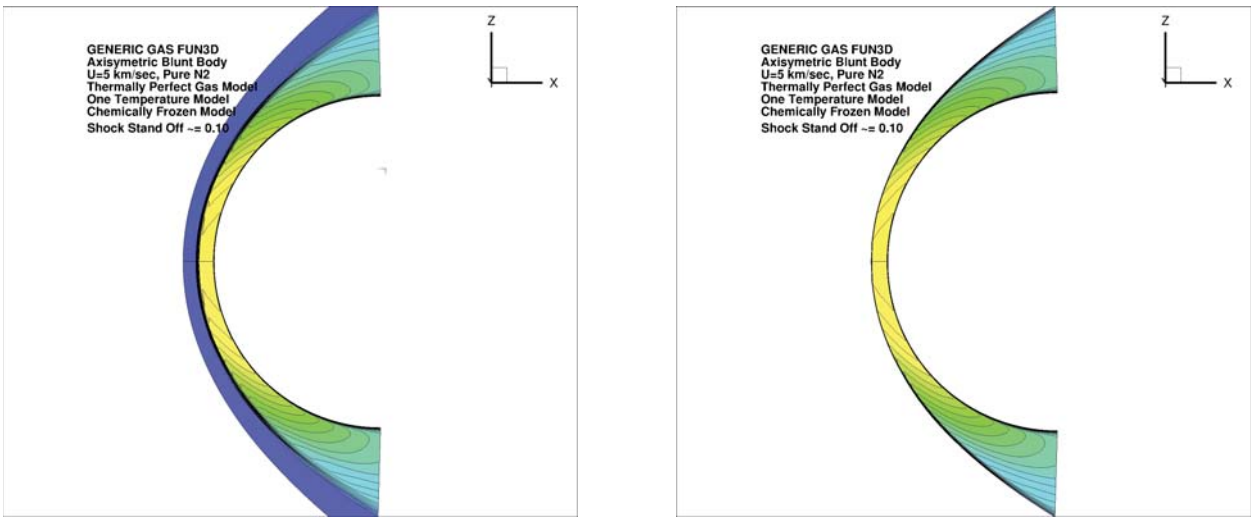

(a) Captured shock.

(b) Fitted shock.

Figure 19: A comparison of shock captured and shock fitted solutions around a spherical blunt body.

and the shock speed. The shock speed is used to move the free stream boundary grid nodes in psuedo-time and the solution of the linear elasticity equations will ultimately be used to move the remaining grid nodes such that they remain conformal to the other surfaces and the interior of the computational domain. Initial testing of shock fitting boundary conditions and grid motion strategies have utilized a preexisting hex-grid-based line-adaptation algorithm to iteratively move the free stream boundary until it fits the bow shock shape. Figure 19 presents a comparison of the static temperature contours from a very preliminary initial test of a shock fitted solution with a shock captured solution for 5 km/sec flow of chemically frozen, thermally perfect N2 over a spherical blunt body.

B. Reconstruction with segmented basis functions

As noted earlier, multi-dimensional reconstruction provides significant improvement to simulations of hypersonic flow on tetrahedral grids. Solution quality of surface heating is still not as good as that obtained using well aligned, hexahedral grids. Sensitivity of the solution to the algorithm detecting a shock normal direction is observed in the heating. An approach using segmented, orthonormal basis functions is being developed to provide more accurate flux reconstruction within an element that includes a shock with the expectation that basis functions comprised of discontinuous segments spanning the element may provide some advantage when the solution itself is also discontinuous.

As these basis functions were derived a self-mapping property under multiplication became evident in which the product of any two basis functions $g_i(x)g_j(x)$ equals a rescaled basis function $(x_b - x_a)^{-1/2}g_k(x)$ where x_b and x_a are endpoints of the domain. This property greatly simplifies an algorithm to obtain the series solutions of non-linear differential equations. A separate paper on this topic is currently under review. Some preliminary results follow to highlight how this method may impact reconstruction algorithms in FUN3D.

The equations defining steady, quasi-one-dimensional flow through a nozzle are

$$\frac{\partial \rho u A}{\partial x} = 0 \tag{10}$$

$$\frac{\partial (\rho u^2 A + pA)}{\partial x} = pA\frac{1}{A}\frac{\partial A}{\partial x} \tag{11}$$

$$\frac{\partial \rho u H A}{\partial x} = 0 \tag{12}$$

where primitive, dimensionless variables are density ρ, velocity u, pressure p, and internal energy e. The total enthalpy H is defined $H = e + p/\rho + u^2/2$. The equation of state for a perfect gas is $p = (\gamma - 1)\rho e$ where the ratio of specific heats for air as a perfect gas is $\gamma = 1.4$. A superscript * indicates a dimensional quantity. Pressure and total enthalpy are non-dimensionalized by their respective values in the nozzle

plenum; consequently $p_{plen} = 1$ and $H_{plen} = 1$. Density is non-dimensionalized by $\rho^* = p^*_{plen}/H^*_{plen}$ so that $\rho_{plen} = \gamma/(\gamma - 1)$. Velocity is non-dimensionalized by $\sqrt{H^*_{plen}}$. Distance from the nozzle throat x^* is non-dimensionalized by the distance to the exit plane x^*_{exit}. The nozzle area distribution $A(x)$ used herein is defined

$$A(x) = A_{throat} + \frac{1}{2}\left(1 - \cos(\pi x)\right) \qquad -1 \le x \le 1 \tag{13}$$

A nozzle schematic with boundary conditions is shown in Fig. 20. Two inflow boundary conditions at $x = x_a = -1$ match total enthalpy and isentropic flow from the plenum. A single outflow boundary condition at $x = x_b = 1$ matches pressure at the exit plane.

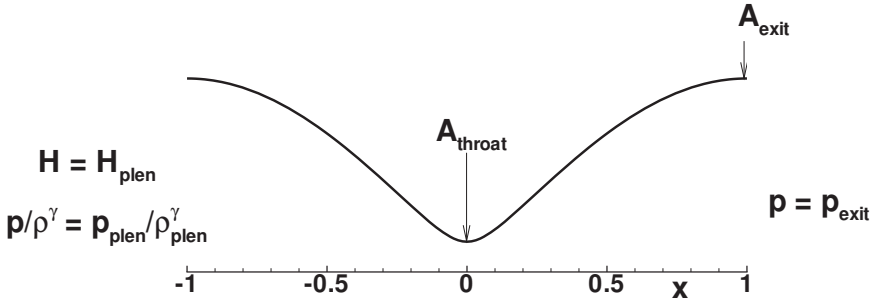

Figure 20: Schematic of nozzle geometry and boundary conditions.

Analytic solutions to nozzle flow can be defined as a function of area ratio.[38] The nozzle has $A_{throat} = A(0) = .05$ and $A_{exit} = A(1) = 1.05$. In this geometry, if $1 > p_{exit} > 0.9994681$ then the flow throughout the nozzle is subsonic. If $0.9994681 > p_{exit} > 0.064722579$ then the flow is sonic at the throat and a shock stands between the throat and the exit. A simulation with $p_{exit} = 0.1$ is presented in Fig. 21. The solution to Eqs. (10 - 12) is comprised of basis function representations of

$$\begin{aligned}
\rho(x)A(x) &= \sum_{n=1}^{128} Q_{1,n} g_n(x) \\
\rho(x)u(x)A(x) &= \sum_{n=1}^{128} Q_{2,n} g_n(x) \\
\rho(x)E(x)A(x) &= \sum_{n=1}^{128} Q_{3,n} g_n(x)
\end{aligned}$$

across the nozzle. The exact solution for pressure is shown in red and for Mach number is shown in blue. The shock is captured as a discontinuity at the correct location in the nozzle. The nozzle domain is not explicitly discretized and the solution is derived only as a function of basis function components. The segmented nature of the basis function solution is retained in the presentation of the solution (black lines) in Fig. 21.

Extending this approach to systems of equations in 2 or more directions will be studied for the purpose of improving simulations on tetrahedral elements – exploiting the ability to capture discontinuities without occurrence of Gibbs phenomena.

IX. Summary

The functional equivalence of the unstructured grid code FUN3D to the the structured grid code LAURA (Langley Aerothermodynamic Upwind Relaxation Algorithm) is documented for applications of interest to the Entry, Descent, and Landing (EDL) community. Examples from an existing suite of regression tests are used to demonstrate the functional equivalence, encompassing various thermochemical models and vehicle configurations. Figures are presented in which a ±4% LAURA band is defined for surface pressures and heating. In all cases with attached flow FUN3D pressures go through the center of the band – indicating excellent agreement with LAURA. In most cases with attached flow FUN3D convective heating is bounded

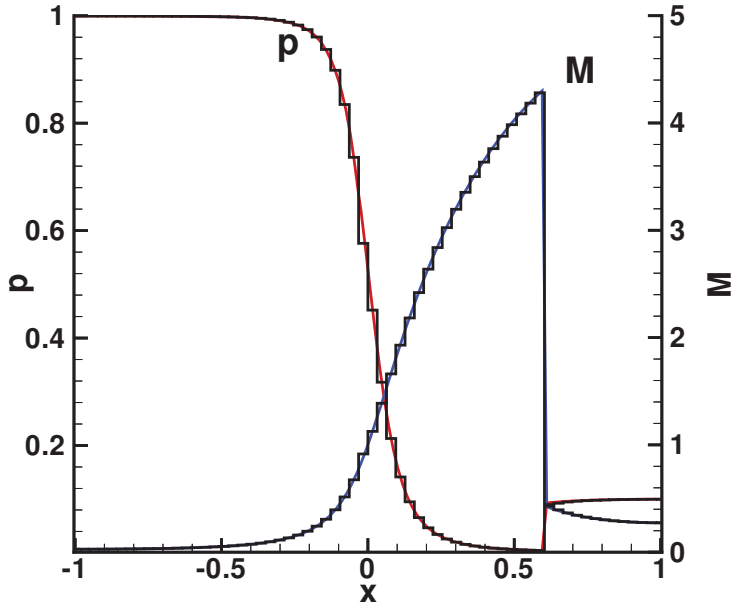

Figure 21: Series solution to supersonic nozzle flow with a standing shock in the nozzle for $A_{exit}/A_{throat} = 21$, 128 basis function components, and $p_{exit} = 0.1$. The exact solution for pressure (red) and exact solution for Mach number (blue) compared to series solution (black).

by the 4% band or skirts the upper limit of the band in the stagnation region. Radiative heating from the FUN3D–HARA coupling is in very good agreement with the LAURA–HARA coupling for a Fire II test case. Cases with significant amounts of separated flow showed larger functional differences between FUN3D and LAURA for both pressure and heating. While some discussion of the role of eigenvalue limiting in these differences is provided – especially for the separated flow case – more work is required to isolate if the differences are caused by numerical parameters, a failure to achieve grid convergence in the separated zone, or both.

Algorithm modifications required for the node-based unstructured grid code (FUN3D) to reproduce functionality of the cell-centered structured code (LAURA) are also documented. These algorithm modifications substantially involve boundary condition formulation (with and without availability of ghost cells) and implementation of eigenvalue limiting when orientation of a cell face relative to the boundary layer cannot be assumed based on a structured (i, j, k) ordering of cells. Challenges associated with computation on tetrahedral grids versus computation on structured-grid derived hexahedral systems are discussed and some innovative ideas are introduced to deal with these challenges.

X. Acknowledgements

This work is funded by the Hypersonics Entry, Descent and Landing (HEDL) Project within NASA's Game Changing Development Program.

References

[1]Mazaheri, A., Gnoffo, P. A., Johnston, C. O., and Kleb, B., "LAURA Users Manual: 5.3-48528," NASA TM 216836, August 2010.

[2]Gnoffo, P. A., "Code Calibration Program in Support of the Aeroassist Flight Experiment," *J. Spacecraft and Rockets*, Vol. 27, No. 2, March-April 1990, pp. 131–142.

[3]Wright, M. J., Candler, G. V., and Bose, D., "Data-Parallel Line Relaxation Method for the Navier-Stokes Equations," *AIAA J.*, Vol. 36, No. 9, 1998, pp. 1603–1609.

[4]Gnoffo, P. A., "Multi–Dimensional, Inviscid Flux Reconstruction for Simulation of Hypersonic Heating on Tetrahedral Grids," AIAA Paper 2009–0599, Jan. 2009.

[5]Gnoffo, P. A., "Updates to Multi–Dimensional Flux Reconstruction for Hypersonic Simulations on Tetrahedral Grids,"

AIAA Paper 2010–1271, Jan. 2010.

[6]Anderson, W. K. and Bonhaus, D. L., "An Implicit Upwind Algorithm for Computing Turbulent Flows on Unstructured Grids," *Comp. and Fluids*, Vol. 23, No. 1, Jan. 1994, pp. 1–21.

[7]Barth, T. J. and Jesperson, D. C., "The Design and Application of Upwind Schemes on Unstructured Meshes," AIAA Paper 89–0366, Jan. 1989.

[8]White, J. A. and Morrison, J. H., "A Pseudo-Temporal Multi-Grid Relaxation Scheme for Solving the Parabolized Navier-Stokes Equations," AIAA Paper 99–3360, June 1999.

[9]Roe, P. L., "Approximate Riemann Solvers, Parameter Vectors, and Difference Schemes," *J. Comput. Phys.*, Vol. 43, No. 2, Oct. 1981, pp. 357–372.

[10]Yee, H. C., "On Symmetric and Upwind TVD Schemes," NASA TM 88325, 1986.

[11]Gnoffo, P. A., Gupta, R. N., and Shinn, J. L., "Conservation Equations and Physical Models for Hypersonic Air Flows in Thermal and Chemical Nonequilibrium," NASA TP 2867, Feb. 1989.

[12]Harten, A., "High Resolution Schemes for Hyperbolic Conservation Laws," *J. Comput. Phys.*, Vol. 49, 1983, pp. 357–393.

[13]Quirk, J. J., "A Contribution to the Great Riemann Solver Debate," *Int. J. Numer. Meth. Fluids*, Vol. 18, 1994, pp. 555–574.

[14]Robinet, J.-C., Gressier, J., Casalis, G., and Moschetta, J.-M., "Shock wave instability and the carbuncle phenomenon: same intrinsic origin?" *J. Fluid Mech.*, Vol. 417, 2000, pp. 237–263.

[15]Alexandrov, N., Atkins, H. L., Bibb, K. L., Biedron, R. T., Gnoffo, P. A., Hammond, D. P., Jones, W. T., Kleb, W. L., Lee-Rausch, E. M., , Nielsen, E. J., Park, M. A., Raman, V. V., Roberts, T. W., Thomas, J. L., Vatsa, V. N., Viken, S. A., White, J. A., and Wood, W. A., "Team Software Development for Aerothermodynamic and Aerodynamic Analysis and Design," NASA/TM 2003-212421, Nov. 2003.

[16]Johnston, C. O., Mazaheri, A., Gnoffo, P., Kleb, B., and Bose, D., "Radiative Heating Uncertainty for Hyperbolic Earth Entry, Part 1: Flight Simulation Modeling and Uncertainty," *J. Spacecraft and Rockets*, Vol. 50, No. 1, 2013, pp. 19–38.

[17]Hash, D., Olejniczak, J., Wright, M., Prabhu, D., Pulsonetti, M., Hollis, B., Gnoffo, P., Nompelis, M. B. I., and Candler, G., "FIRE II Calculations for Hypersonic Nonequilibrium Aerothermodynamics Code Verification: DPLR, LAURA, and US3D," AIAA Paper 2007–605, Jan. 2007.

[18]Gnoffo, P. A., Hartung, L. C., and Greendyke, R. B., "Heating Analysis for a Lunar Transfer Vehicle at Near-Equilibrium Flow Conditions," AIAA Paper 93-0270, Jan. 1993.

[19]Gnoffo, P. A., "CFD Validation Studies for Hypersonic Flow Prediction," AIAA Paper 2001-1025, Jan. 2001.

[20]Weilmuenster, K. J. and Gnoffo, P. A., "Solution Strategy for Three-Dimensional Configurations at Hypersonic Speeds," *J. Spacecraft and Rockets*, Vol. 30, No. 4, July-August 1993, pp. 385–394.

[21]Gnoffo, P. A. and Weilmuenster, K. J., "Multiblock Analysis for Shuttle Orbiter Re-Entry Heating from Mach 24 to Mach 12," AIAA Paper 93-2813, July 1993.

[22]McIntyre, T. J., Bishop, A. I., Rubinsztein-Dunlop, H., and Gnoffo, P. A., "Comparison of Experimental and Numerical Studies of Ionizing Flow over a Cylinder," *AIAA J.*, Vol. 41, No. 11, Nov. 2003, pp. 2157–2161.

[23]Cebeci, T. and Smith, A. M. O., "A Finite-Difference Method for Calculating Compressible Laminar and Turbulent Boundary Layers," *J. Basic Eng.*, Sept. 1970, pp. 523–535.

[24]Gnoffo, P. A., Berry, S. A., and Norman, J. W., "Uncertainty Assessments of Hypersonic Shock Wave - Turbulent Boundary Layer Interactions at Compression Corners," *J. Spacecraft and Rockets*, Vol. 50, No. 1, Jan. 2013, pp. 69–95.

[25]Gnoffo, P., Johnston, C., and Thompson, R., "Implementation of Radiation, Ablation, and Free Energy Minimization Modules for Coupled Simulations of Hypersonic Flow," *J. Spacecraft and Rockets*, Vol. 47, No. 2, 2010, pp. 251–257.

[26]Gnoffo, P. A., Weilmuenster, K. J., and Alter, S. J., "Multiblock Analysis for Shuttle Orbiter Re-Entry Heating from Mach 24 to Mach 12," *J. Spacecraft and Rockets*, Vol. 31, No. 3, May 1994, pp. 367–377.

[27]Weilmuenster, K. J., Gnoffo, P. A., and Greene, F. A., "Navier-Stokes Simulations of Orbiter Aerodynamic Characteristics Including Pitch Trim and Bodyflap," *J. Spacecraft and Rockets*, Vol. 31, No. 3, May 1994, pp. 355–366.

[28]Gnoffo, P. A. and Alter, S. J., "Simulation of Flow Through Breach in Leading Edge at Mach 24," AIAA Paper 2004–2283, June 2004.

[29]Stewart, D. A., "Surface Catalysis and Characterization of Proposed Candidate TPS for Access-to-Space Vehicles," NASA TM 112206, July 1997.

[30]John H. Lewis, J. and Scallion, W. I., "Flight Parameters and Vehicle Performance for Project FIRE Flight II, Launched May 22, 1965," TN, NASA, August 1966.

[31]Cauchon, D. L., "Radiative Heating results from the FIRE II Flight Experiment at a Rentry Velocity of 11.4 Kilometers per Second," TM, NASA, July 1967.

[32]Wood, W. A., "Radiation Coupling with the FUN3D Unstructured-Grid CFD Code," AIAA Paper 2012-2741, June 2012.

[33]Sutton, K. and Gnoffo, P. A., "Multi-component Diffusion with Application to Computational Aerothermodynamics," AIAA Paper 98–2575, June 1998.

[34]Wilcox, D. C., *Turbulence Modeling for CFD, Third Edition*, DCW Industries, Inc., La Cañada, CA, 2006.

[35]Holden, M., MacLean, M., Wadhams, T., and Mundy, E., "Experimental Studies of Shock Wave/Turbulent Boundary Layer Interaction in High Reynolds Number Supersonic and Hypersonic Flows to Evaluate the Performance of CFD Codes," AIAA Paper 2010–4468, June 2010.

[36]Gnoffo, P. A., Berry, S. A., and Norman, J. W. V., "Uncertainty Assessments of Hypersonic Shock Wave-Turbulent Boundary-Layer Interactions at Compression Corners," *J. Spacecraft and Rockets*, Vol. 50, No. 1, 2013, pp. 69–95.

[37]Bonfiglioli, A., Grottadaurea, M., Paciorri, R., and Sabetta, F., "An Unstructured, Three-Dimensional, Shock-Fitting Solver for Hypersonic Flows," *Comp. and Fluids*, Vol. 73, March 2013, pp. 162–174.

[38]Ames Research Staff, "Equations, Tables, and Charts for Compressible Flow," NACA TR 1135, 1953.